

NUCLEAR X-RAY PROPERTIES OF THE PECULIAR RADIO-LOUD HIDDEN AGN 4C+29.30

M. A. SOBOLEWSKA¹, ANETA SIEMIGINOWSKA¹, G. MIGLIORI¹, Ł. STAWARZ^{2,3}, M. JAMROZY³, D. EVANS¹, AND C. C. CHEUNG⁴

¹ Harvard-Smithsonian Center for Astrophysics, 60 Garden Street, Cambridge, MA 02138, USA; msobolewska@cfa.harvard.edu

² Institute of Space and Astronautical Science, JAXA, 3-1-1 Yoshinodai, Sagami-hara, Kanagawa 229-8510, Japan

³ Astronomical Observatory, Jagiellonian University, ul. Orła 171, 30-244 Kraków, Poland

⁴ National Research Council Research Associate, National Academy of Sciences, Washington, DC 20001, USA,
resident at Naval Research Laboratory, Washington, DC 20375, USA

Received 2012 April 5; accepted 2012 August 20; published 2012 October 3

ABSTRACT

We present results from a study of nuclear emission from a nearby radio galaxy, 4C+29.30, over a broad 0.5–200 keV X-ray band. This study used new *XMM-Newton* (~ 17 ks) and *Chandra* (~ 300 ks) data, and archival *Swift*/BAT data from the 58 month catalog. The hard (> 2 keV) X-ray spectrum of 4C+29.30 can be decomposed into an intrinsic hard power law ($\Gamma \sim 1.56$) modified by a cold absorber with an intrinsic column density $N_{\text{H},z} \sim 5 \times 10^{23} \text{ cm}^{-2}$, and its reflection ($|\Omega/2\pi| \sim 0.3$) from a neutral matter including a narrow iron $K\alpha$ emission line at a rest-frame energy ~ 6.4 keV. The reflected component is less absorbed than the intrinsic with an upper limit on the absorbing column of $N_{\text{H},z}^{\text{refl}} < 2.5 \times 10^{22} \text{ cm}^{-2}$. The X-ray spectrum varied between the *XMM-Newton* and *Chandra* observations. We show that a scenario invoking variations of the normalization of the power law is favored over a model with variable intrinsic column density. X-rays in the 0.5–2 keV band are dominated by diffuse emission modeled with a thermal bremsstrahlung component with temperature ~ 0.7 keV, and contain only a marginal contribution from the scattered power-law component. We hypothesize that 4C+29.30 belongs to a class of “hidden” active galactic nuclei containing a geometrically thick torus. However, unlike the majority of hidden AGNs, 4C+29.30 is radio-loud. Correlations between the scattering fraction and Eddington luminosity ratio, and between black hole mass and stellar velocity dispersion, imply that 4C+29.30 hosts a black hole with $\sim 10^8 M_{\odot}$ mass.

Key words: accretion, accretion disks – galaxies: active – galaxies: individual (4C+29.30) – X-rays: galaxies

Online-only material: color figures

1. INTRODUCTION

4C+29.30 is a low-redshift ($z = 0.0647$) radio source with a moderate radio luminosity $\sim 10^{42} \text{ erg s}^{-1}$ (Siemiginowska et al. 2012) hosted by an elliptical galaxy. It was first studied in the radio and optical bands by van Breugel et al. (1986). Observed complex radio morphology was resolved into jets, knots, lobes, and a diffuse tail. A number of optical emission lines were measured, and their relative intensities indicated photoionization by a non-stellar continuum attributed to the central active galactic nucleus (AGN). The radio emission and the optical line emitting gas were found to be strongly linked, suggesting interaction between the radio source and its environment. In addition, shells and dust lanes observed in the optical band (van Breugel et al. 1986) provide evidence of a past merger with a gas-rich disk galaxy which possibly triggered the rejuvenated AGN activity. Subsequently, follow-up radio studies revealed radio structures with diverse spectral ages suggesting an intermittent nature of the radio source in 4C+29.30. Jamrozy et al. (2007) presented evidence for a large-scale extended relic radio emission most probably due to an earlier cycle of activity of the source $\gtrsim 200$ Myr ago. The age of a small-scale radio structure embedded in the extended relic radio emission was estimated at $\lesssim 100$ Myr, with the inner double knots of a spectral age of $\lesssim 33$ Myr (Jamrozy et al. 2007). Liuzzo et al. (2009) resolved the very central region of the source into two nuclear knots with spectral ages of ~ 15 yr and ~ 70 yr. 4C+29.30 was cataloged as an infrared point source by *IRAS*, *WISE*, and the Two Micron All Sky Survey (2MASS) (NASA/IPAC Infrared Science Archive).

The first detection of the source in the X-ray band occurred during a snapshot 8 ks *Chandra* observation (Gambill et al. 2003). The short exposure time and few detected counts prevented detailed spectral analysis. Nevertheless, this pilot observation hinted at a complex X-ray morphology composed of a nucleus, hotspots, a putative jet, and diffuse emission. The source was not a target of X-ray pointings prior to the first *Chandra* observation, without detection in, e.g., the ROSAT All Sky Survey, probably due to significant intrinsic absorption (Gambill et al. 2003; Siemiginowska et al. 2012). In 2008, we observed 4C+29.30 with *XMM-Newton* for ~ 45 ks. This observation was followed by our deep 300 ks *Chandra* exposure (Siemiginowska et al. 2012, hereafter Paper I) which clearly revealed diverse X-ray-emitting structures, many of which correspond to those in radio or optical bands, and others are intrinsic to the X-ray band. The soft 0.5–2 keV X-ray image showed northern and southern lobes, hotspots, a southern jet, and thermal diffuse emission in the center. Emission in the hard X-ray band (above 2 keV) was instead dominated by the active nucleus of 4C+29.30. In Paper I, our discussion focused on the spectral properties of the soft X-ray components, the structure of the outflow, and interactions of the X-ray jet with the interstellar medium (ISM). We emphasized similarities between 4C+29.30 and famous radio galaxies showing jet–ambient-medium interactions, i.e., M87 (e.g., Million et al. 2010), NGC 1275 (e.g., Fabian et al. 2011), and Cen A (e.g., Morganti 2010 and references therein).

In the present paper, we focus on detailed modeling of the X-ray core emission to uncover the nature of the AGN powering 4C+29.30. We analyze new *Chandra* data and archival

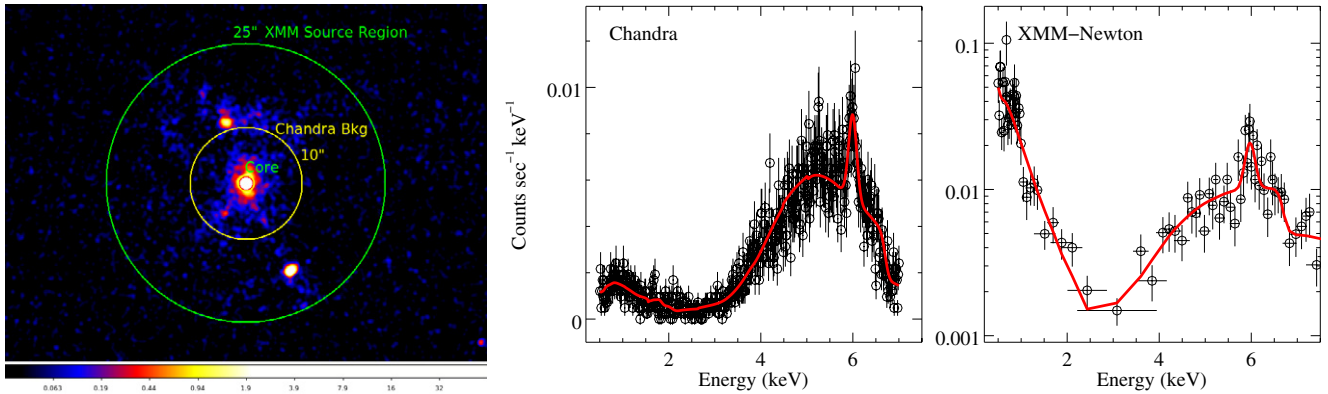


Figure 1. Left: extraction regions for 4C+29.30 core spectra in the *Chandra* and *XMM-Newton* observations ($1''.25$ magenta and $25''$ green circles, respectively), and $10''$ *Chandra* background overlaid on top of our deep *Chandra* image. The ACIS-S *Chandra* image has been filtered and includes only 0.5–7 keV photons. The original ACIS pixels were binned to $0''.123$ and smoothed with Gaussian function of $\sigma = 0''.615$. Middle: unbinned *Chandra* spectrum of the $1''.25$ core region and folded Model 3 (see Section 3.1). Right: *XMM-Newton* spectrum of the $25''$ source region and folded Model 3b (see Section 3.2). (A color version of this figure is available in the online journal.)

Swift/BAT data from the 58 month catalog (Baumgartner et al. 2010), and thus we study the core emission over a broad 0.5–200 keV X-ray band. We apply our best-fit model to our new *XMM-Newton* observations of 4C+29.30 taken ~ 2 years before our *Chandra* observation. We search for signatures of the X-ray spectral variability between the *Chandra* and *XMM-Newton* observations. The paper is organized as follows. In Section 2 we describe our data and provide details on the preparation of the spectra for modeling. In Section 3 we test various spectral scenarios for AGN X-ray activity. We compare the best-fitting *Chandra* and *XMM-Newton* models in order to study the origins of possible spectral variability. In Section 4 we present the discussion of our results indicating that 4C+29.30 is a strongly absorbed intrinsically X-ray-variable AGN with Seyfert 2 type activity and a peculiar obscuring geometry, probably due to a geometrically thick torus similar to that reported for several *Swift*/BAT-selected AGNs (e.g., Ueda et al. 2007; Winter et al. 2009a, 2009b). Finally, in Section 5 we summarize and conclude our study. Throughout the paper we adopt $\Omega_\Lambda = 0.73$, $\Omega_M = 0.27$, and $H_0 = 70 \text{ km s}^{-1} \text{ Mpc}^{-1}$ for the flux–luminosity transformations.

2. X-RAY OBSERVATIONS

2.1. XMM-Newton

Our *XMM-Newton* observation of 4C+29.30 was performed on 2008 April 11. It was split into two pointings lasting ~ 45.7 ks (ID: 0504120101) and ~ 9.7 ks (ID: 0504120201). No science data were produced during the second pointing. The data reduction of the 45.7 ks observation was performed following the standard procedure⁵ with the XMM-SAS ver. 11.0.0 package using the updated calibration files (2011 October). We constructed light curves at energies above 10 keV to identify periods of high background flaring. After cleaning the data, we obtained the following net exposures and 0.5–10 keV observed count rates: ~ 17 ks and $(6.3 \pm 0.2) \times 10^{-2} \text{ counts s}^{-1}$ for the EPIC/PN camera, ~ 23 ks and $(1.75 \pm 0.09) \times 10^{-2} \text{ counts s}^{-1}$ for MOS1, and ~ 23 ks and $(2.03 \pm 0.09) \times 10^{-2} \text{ counts s}^{-1}$ for MOS2. In this paper we will limit the discussion to the EPIC/PN data which provide better statistics than the MOS data. However, the data taken by the EPIC/MOS1 and MOS2 have been checked for consistency.

The source 0.5–10 keV PN spectrum was extracted from a circular region (centered at R.A. 08:40:02.276, decl. +29:49:02.47, J2000.0) of $25''$ radius (Figure 1), and the background from a circular region located on the same CCD ($50''$ radius, not indicated in Figure 1). The response matrices were created using the SAS commands `rmfgen` and `arfgen`. The source data are not piled-up. We used `specgroup` to set spectral groups such that each group/bin contains a minimum signal-to-noise ratio of 3.

2.2. Chandra

Deep *Chandra* ACIS-S imaging observations of 4C+29.30 were performed in 2010 February, i.e., ~ 2 years after our *XMM-Newton* observation. The approved 300 ks observation was split into four separate pointings (ObsIDs 11688, 11689, 12106, 12119) that sum to a total exposure time of 286.4 ks (see Paper I for details of the observations and data reduction). In this paper we use the four combined⁶ 0.5–7 keV X-ray spectra (5328 ± 73 total counts) of the core region (Figure 1) defined as a circle with radius of $1''.25$ centered at the position of the nucleus determined based on the hard band *Chandra* X-ray image (R.A. 08:40:02.345, decl. +29:49:02.61, J2000.0; Paper I), together with the appropriate calibration response files. The background (25 ± 5 counts) was extracted from an annulus centered on the core position with an inner radius of $1''.5$ and an outer radius of $10''$. We use CIAO version 4.3 tools for the data analysis.

2.3. Swift/BAT

We extend the *Chandra* and *XMM-Newton* energy band-passes by considering the publicly available 14–195 keV (eight-channel) hard X-ray *Swift*/BAT spectrum from the 58 month catalog (between 2004 November and 2008 September; Baumgartner et al. 2010) together with the corresponding response matrix `diagonal_8.rsp`. We do not detect any long-term variability signal in the *Swift*/BAT light curve (normalized excess variance $\sigma_{\text{NXS}}^2 < 0$; e.g., Vaughan et al. 2003). Either way, integrating the data over the period of ~ 5 years would smear any hard X-ray spectral variations. Thus, the *Swift*/BAT data are representative of the average hard X-ray emission from 4C+29.30.

⁶ Because the data were collected on the same part of the ACIS-S detector and spanned a relatively short time interval, we used the CIAO 4.3 script `combine_spectra` to combine individual spectra and response files into one spectrum for this analysis.

⁵ <http://xmm.esac.esa.int/sas/current/documentation/threads/>

Table 1
XSPEC/Sherpa Terminology of the Spectral Models

Name	Description
Model 1 ^a	phabs * (zbremss + zphabs*CPL)
Model 2	phabs * (zbremss + zphabs*CPL + zgauss)
Model 3	phabs * (zbremss + zphabs*CPL + zgauss + pexriv)
Model 4	phabs * (zbremss + zphabs*CPL + zgauss + zphabs*pexriv)
Model 5 ^b	phabs * (zbremss + zpcfabs*CPL + zgauss + zphabs*pexriv)
Model 6 ^c	phabs * (zbremss + zphabs*CPL + constant*CPL + zgauss + zphabs*pexriv)
Model 7 ^c	phabs * (zphabs*CPL + constant*CPL + zgauss + zphabs*pexriv)

Notes. Models 4–6 converged to Model 3. In Sherpa the individual model names are preceded by xs.

^a CPL \equiv zhighect * zpowerlw.

^b zpcfabs \equiv f_{pc} *zphabs + (1 - f_{pc}).

^c constant \equiv f_{sc} .

3. MODELING

In this section we use our deep *Chandra* observation to establish a spectral model for the 4C+29.30 core continuum. We use the *Swift*/BAT data to check the consistency of the model with X-ray data outside the *Chandra* energy bandpass. Finally, we apply the best-fitting *Chandra* model to the *XMM-Newton* observation taken ~ 2 years prior to the *Chandra* pointing, and we discuss the X-ray spectral variability of the source. We perform the fits in *Sherpa* (Freeman et al. 2001) using CSTAT statistic.

The *Swift*/BAT data were averaged over 58 months of observations, which potentially might introduce a discrepancy between the *Chandra* (or *XMM-Newton*) and *Swift*/BAT data due to the X-ray flux variability. *Swift*/BAT composite spectra contain fractional counts with Gaussian statistics and are background subtracted, which prevents CSTAT fitting.⁷ For this reason, we find the best fit of each model to the *Chandra* (or *XMM-Newton*) data only. Then we apply the best-fit model to the *Swift*/BAT data using the χ^2 statistic with variance supplied by the data `chi2specvar`, allowing for only one free parameter, the normalization constant, C_{BAT} .

Table 1 contains the description of all models used in the paper in the XSPEC (Arnaud 1996) and Sherpa terminology. In Table 2 we list the best-fit model parameters and the resulting fit statistics. All models considered in this section include Galactic absorption (phabs) with a column density fixed at $N_{\text{H}} = 3.98 \times 10^{20} \text{ cm}^{-2}$ (Dickey & Lockman 1990). Errors on the spectral parameters correspond to the 68% confidence level (1σ) for one significant parameter.

A region of the diffuse emission surrounding the nucleus can be clearly identified in the soft 0.5–2 keV *Chandra* image (“Center” in Figure 2 in Paper I). In Paper I, we showed that a thermal bremsstrahlung model provided a better fit to the spectra extracted from this region than a power-law model. Thus, all our models include a thermal bremsstrahlung component with the temperature and normalization allowed to vary.

We modeled the *Chandra* and *XMM-Newton* background spectra by fitting appropriate background regions (Figure 1) with a model consisting of a Galactic absorption, thermal bremsstrahlung, and power law. The background model parameters are listed in Table 2. The parameters differ because the *XMM-Newton* background was collected from a region at the distance $>25''$ from the nucleus.

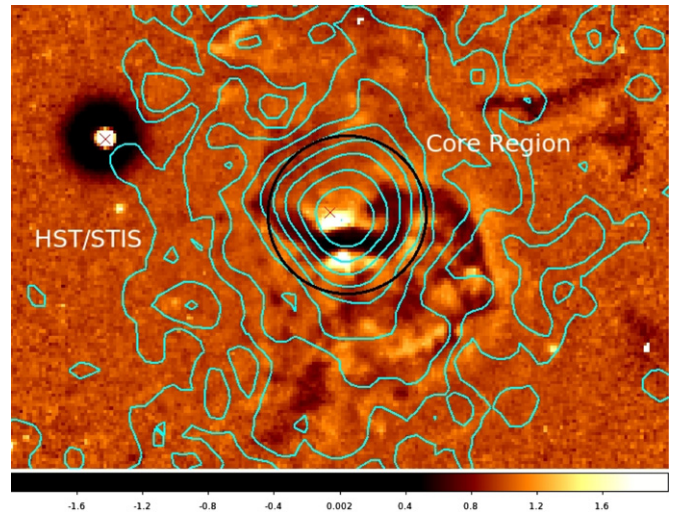


Figure 2. Unsharp mask optical *HST* image of 4C+29.30 with overlaid *Chandra* X-ray contours (cyan; Paper I). The crosses indicate the optical SDSS identified counterparts. The $1'25$ *Chandra* core extraction region is indicated (black circle). A dust lane across the optical nucleus is clearly visible.

(A color version of this figure is available in the online journal.)

3.1. *Chandra*

We considered several models for the nuclear X-ray emission of 4C+29.30 observed with *Chandra*.

Model 1. First, we tried a simple parameterization using a cutoff power-law function (zhighect*zpowerlw in XSPEC terminology; in the following we will refer to this component as CPL or “a power law”). The zhighect model is defined as $\exp[E_1/E_{\text{fold}} - E \times (1+z)/E_{\text{fold}}]$. We assumed $E_1 = 0$. The E -folding energy, E_{fold} , could not be constrained by our data and we fixed it at 300 keV. We added an intrinsic absorber with a variable column density (zphabs), motivated by the presence of a dust line crossing the nuclear region, as revealed by the *Hubble Space Telescope* (*HST*) image (Figure 2). We were not able to obtain a good fit with this model. The plot of the model-to-data ratio revealed residuals in the 5–7 keV band suggesting the presence of an iron $K\alpha$ emission line (Figure 3(a)). These residuals forced the photon index of the intrinsically absorbed ($N_{\text{H},z} \sim 4 \times 10^{23} \text{ cm}^{-2}$) continuum to converge to an unusually low value, $\Gamma = 0.84^{+0.11}_{-0.27}$.

Model 2. In Model 2 we added a Gaussian line (zgauss) which reduced the 5–7 keV residuals significantly (Figure 3(b)). The resulting line was narrow, $\sigma = (0.07 \pm 0.03) \text{ keV}$, and centered at the rest-frame energy of $E_{K\alpha} = (6.36 \pm 0.02) \text{ keV}$.

⁷ <http://heasarc.nasa.gov/docs/swift/analysis/threads/batspectrumthread.html>

Table 2
Results of Spectral Fits to the *Chandra*, *XMM-Newton*, and *Swift*/BAT Data

	Thermal Bremsstrahlung ^a		Intrinsic Absorption	Cutoff Power Law ^b (CPL)		Fe K α line ^c			Neutral Reflection	Norm. ^d	CSTAT		
	kT (keV)	N_{TB}	$N_{H,z}$ (10^{23} cm $^{-2}$)	Γ	N_{CPL}	E (keV)	ΔE (keV)	EW_o (eV)	EW_i (eV)	$ \Omega/2\pi $	C_{BAT}	Value	Prob. (dof)
<i>Chandra</i>													
Bkg	0.63 ± 0.04	$3.01^{+0.30}_{-0.27}$...	-2.28 ± 0.22	$0.0035^{+0.0016}_{-0.0011}$	578	1 (442)
Model 1	$6.4^{+6.5}_{-2.1}$	$0.46^{+0.04}_{-0.02}$	4.08 ± 0.29	$0.84^{+0.11}_{-0.27}$	27^{+18}_{-11}	0.20 ± 0.03	1129	$\sim 10^{-7}$ (887)
Model 2	$5.2^{+3.0}_{-1.5}$	0.46 ± 0.02	$3.91^{+0.16}_{-0.09}$	$0.97^{+0.07}_{-0.03}$	31^{+21}_{-12}	6.36 ± 0.02	0.07 ± 0.03	192^{+54}_{-37}	91^{+27}_{-18}	...	0.30 ± 0.05	1045	$\sim 10^{-4}$ (884)
Model 3	$0.71^{+0.15}_{-0.12}$	$0.83^{+0.21}_{-0.16}$	4.96 ± 0.14	$1.56^{+0.15}_{-0.04}$	103^{+39}_{-50}	6.36 ± 0.01	0.06 ± 0.03	173^{+62}_{-35}	71^{+27}_{-15}	$0.32^{+0.05}_{-0.13}$	0.68 ± 0.10	1016	0.002 (883)
<i>XMM-Newton</i>													
Bkg	$1.62^{+2.24}_{-0.81}$	$1.34^{+0.45}_{-0.20}$...	$-0.37^{+0.35}_{-0.48}$	$0.13^{+0.13}_{-0.08}$	1219	1 (1903)
Model 3a	0.60 ± 0.07	$8.5^{+1.4}_{-1.1}$	7.88 ± 0.26	1.56^e	103^e	6.36^e	0.06^e	247 ± 10	64	0.32^e	0.68 ± 0.10	228	0.03 (191)
Model 3b	0.60 ± 0.07	$8.7^{+1.4}_{-1.1}$	4.96^e	1.56^e	52.0 ± 2.7	6.36^e	0.06^e	280 ± 13	122 ± 6	0.32^e	1.10 ± 0.16	209	0.30 (191)

Notes.

^a Normalization of the thermal bremsstrahlung, N_{TB} , in units $10^{-5} \times [3.02 \times 10^{-15} / (4\pi D^2(1+z)^2)] \times \int n_e n_i dV$, where n_e is the electron density in cm $^{-3}$, n_i is the ion density in cm $^{-3}$, D is the angular size distance in cm, and z is the redshift.

^b Normalization of the cutoff power law, N_{CPL} , in units 10^{-5} photons keV $^{-1}$ cm $^{-2}$ s $^{-1}$ at 1 keV.

^c The observed (intrinsic) equivalent width EW_o (EW_i) calculated relative to the intrinsically absorbed (unabsorbed) continuum.

^d Normalization constant between the *Chandra* (*XMM-Newton*) and *Swift*/BAT models.

^e Parameter fixed at the Model 3 value.

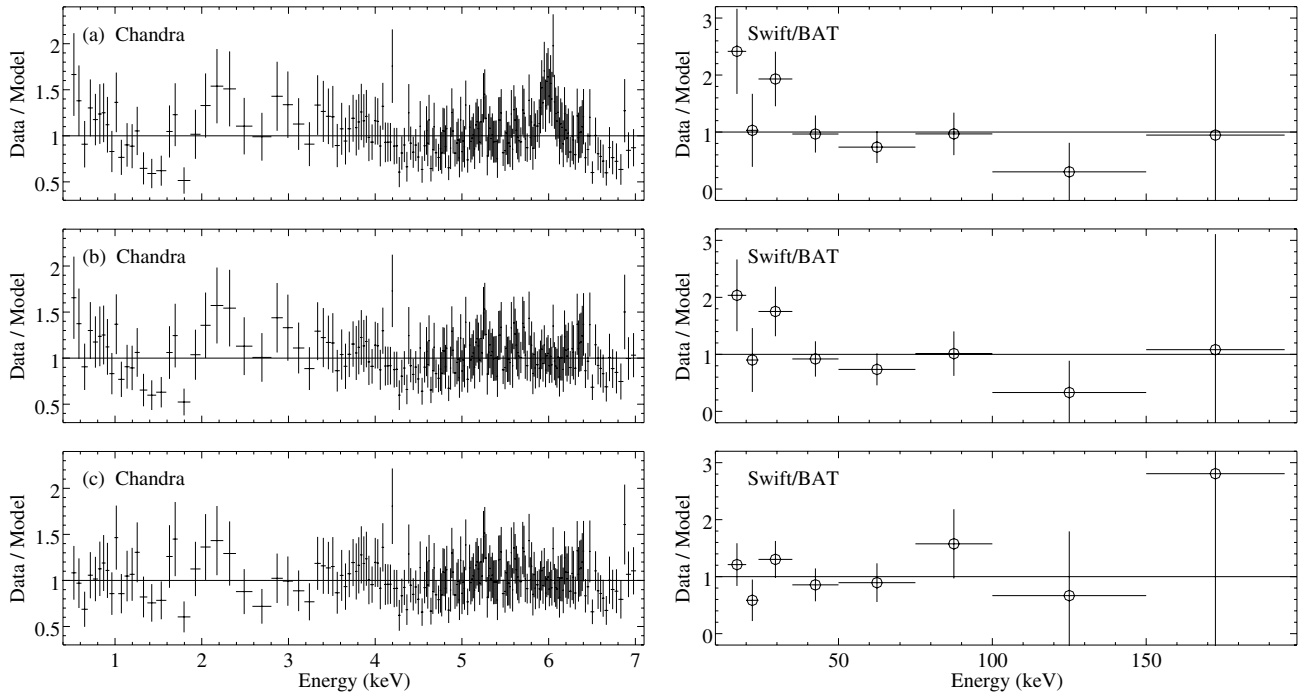


Figure 3. Ratio of the *Chandra* and *Swift*/BAT data to different spectral models. *Chandra* data were binned for the clarity of the plot. (a) Model 1: in the *Chandra* band clear signatures of iron $K\alpha$ line are visible around 6 keV (~ 6.4 keV in the rest frame); resulting photon index is in disagreement with the *Swift*/BAT data. (b) Model 2: the ~ 6 keV residuals disappear after including a Gaussian line in the model; the photon index is still too low to agree with the *Swift*/BAT data. (c) Model 3 with a Gaussian line and reflection fits well both the *Chandra* and *Swift*/BAT data.

These parameters suggest that the line originates in a neutral material far from the black hole, e.g., at the outskirts of an accretion disk, or a dusty torus. The earlier short 8 ks *Chandra* observation contained too few counts to detect the line or put an upper limit on its equivalent width (EW; Gambill et al. 2003). Thus, this is the first detection of the iron $K\alpha$ line in 4C+29.30. The observed EW of the line (i.e., relative to the intrinsically absorbed continuum) was $EW_o = 192^{+54}_{-18}$ eV, while the intrinsic one (i.e., relative to the unabsorbed continuum) was $EW_i = 91^{+27}_{-18}$ eV. The photon index in Model 2 was still unusually low, $\Gamma = 0.97^{+0.07}_{-0.03}$, and the intrinsic absorption remained strong with $N_{H,z} \sim 5 \times 10^{23} \text{ cm}^{-2}$. The temperature of the diffuse emission, $kT = 5.2^{+3.0}_{-1.5}$ keV, was in agreement with that measured in Model 1 ($kT = 6.4^{+6.5}_{-2.1}$ keV), but considerably higher than the temperature of the background thermal bremsstrahlung component, $kT = (0.63 \pm 0.04)$ keV.

Model 3. The detection of the iron $K\alpha$ line suggested that the total spectrum may contain a certain contribution of the associated reflected emission. Hence, we considered the reflection model with a slab geometry, *pexriv* of Magdziarz & Zdziarski (1995), i.e., a reflection from an accretion disk. We first assumed that the reflected component is not intrinsically absorbed, contrary to the case of the incident CPL. This corresponds to a scenario in which the CPL continuum is observed through an obscuring material, e.g., a dusty torus, while the reflected emission arrives at the observer unobscured. With default settings the *pexriv* model computes both the incident CPL and the reflected component. However, in order to apply the intrinsic absorber only to the incident CPL, we leave the CPL component in the model, and choose a setting in which the *pexriv* model returns only the reflected component. Consequently, the reflection amplitude, $\Omega/2\pi$, was fitted over a negative range, which physically corresponds to a reflection component with amplitude $|\Omega/2\pi|$.

We linked the photon index and the normalization of the *pexriv* model to those of CPL. The *pexriv* reflection does not account for the iron line emission and so we kept the *zgauss* component explicitly in the model. The viewing angle, i , is not known for our source. However, an upper limit can be calculated based on the jet-to-counterjet flux ratio, J , at 5 GHz (e.g., Urry & Padovani 1995). Sambruna et al. (2004) and Liuzzo et al. (2009) give $J > 29$ and $J > 50$, implying $i < 60^\circ$ (for discrete knots). We fixed i at 45° , assuming that the jet in 4C+29.30 is well aligned with the axis of the accretion disk. We fixed the abundances of elements at the solar value.

The resulting data-to-model residuals are presented in Figure 3(c). The ionization parameter in the *pexriv* model converged to zero. The iron line remained narrow, and centered at the rest-frame energy of $E_{K\alpha} = (6.36 \pm 0.01)$ keV. Its observed $EW_o = 173^{+62}_{-15}$ eV (intrinsic $EW_i = 71^{+27}_{-15}$ eV) was lower than in Model 2. Thus, the properties of the iron line and the reflected emission support the hypothesis that both components originate in a neutral matter located far away from the black hole. The power-law component with a photon index of $\Gamma = 1.56^{+0.15}_{-0.04}$ was absorbed with an intrinsic column density $N_{H,z} \sim 5 \times 10^{23} \text{ cm}^{-2}$. The reflection amplitude yielded an intermediate value of $|\Omega/2\pi| = 0.32^{+0.05}_{-0.13}$. The temperature of the soft diffuse emission, $kT = 0.71^{+0.15}_{-0.12}$ keV, was significantly lower than that in Models 1 and 2 due to the contribution of the reflected component to the soft X-ray band, and slightly higher than (but consistent with) the temperature of the background thermal component. As a final model check we replaced the thermal bremsstrahlung component with an *apec* model. We were able to establish only an upper limit on the value of metal abundances, $A \lesssim 0.01$. It is generally known that low abundances might be an artifact resulting from fitting the mixed temperature plasma where these mixed temperature components cannot be spectrally or spatially resolved (see, e.g., Kim 2012

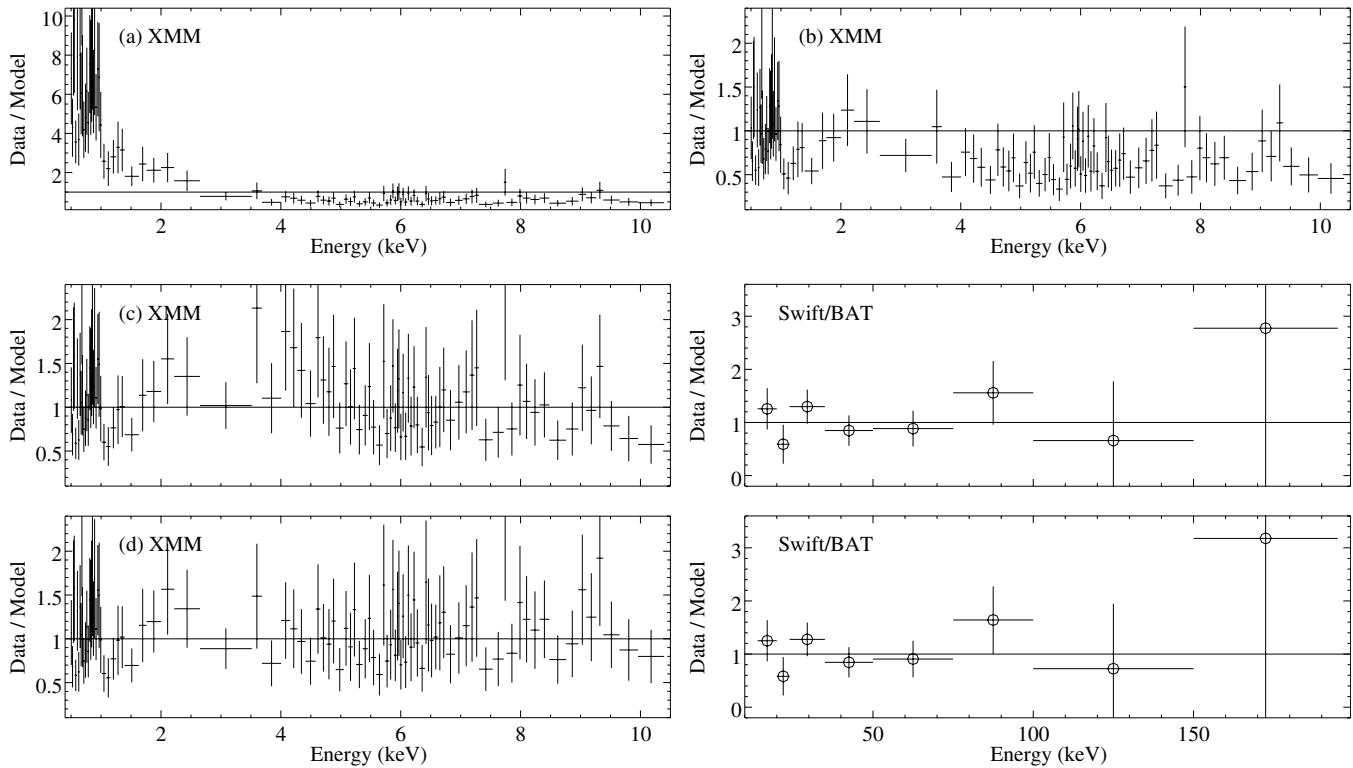


Figure 4. Ratio of the *XMM-Newton* and *Swift/BAT* data to (a) Model 3, best fitting the *Chandra* data; (b) Model 3 with thawed temperature, kT , and normalization, N_{TB} , of the thermal bremsstrahlung component; (c) Model 3a with thawed N_{TB} , kT , and intrinsic absorption column density, $N_{\text{H},z}$; left: *XMM-Newton*; right: *Swift/BAT*; (d) Model 3b, thawed N_{TB} , kT , and normalization of the CPL, N_{CPL} ; left: *XMM-Newton*; right: *Swift/BAT*.

in the context of abundances in hot ISM of elliptical galaxies). This problem with regard to the data of 4C+29.30 was considered in more detail in Siemiginowska et al. (2012). Similar to their approach, we decided to keep the thermal bremsstrahlung component in the model as a good approximation.

Model 4. Next, we allowed for the second intrinsic absorber altering the reflected component with a column density $N_{\text{H},z}^{\text{refl}}$, in addition to the one modifying the intrinsic CPL emission. This model, however, converged to Model 3 with $N_{\text{H},z}^{\text{refl}} = 1.2^{+1.3}_{-1.2} \times 10^{22} \text{ cm}^{-2}$, consistent with zero.

Model 5. Motivated by the studies of other Seyfert 2 type galaxies (e.g., Evans et al. 2007, 2010; Grandi et al. 2007) we tested if a partial covering model (representative for, e.g., a patchy torus) could provide an alternative description of our data. We assumed that only a fraction, f_{pc} (allowed to vary between 0 and 1), of the power-law emission is passing through an obscuring matter, while the remaining fraction $(1-f_{\text{pc}})$ arrives at the observer unabsorbed. This model also converged to Model 3 with $f_{\text{pc}} = 1.0000_{-0.0021}$.

Model 6. Next, we checked if a certain fraction, f_{sc} , of the intrinsic CPL may contribute to the soft emission below 1 keV due to scattering. We found that the scattered component was not formally required by the data with an upper limit on the scattering fraction $f_{\text{sc}} < 0.25 \times 10^{-2}$, thus Model 6 converged to Model 3.

In summary, we conclude that Model 3 accounts properly for the broadband X-ray continuum measured by *Chandra*. In this model, the nuclear radiation described by a cutoff power law with a hard spectrum, $\Gamma \sim 1.56$, is heavily intrinsically absorbed by a cold gas with $N_{\text{H},z} \sim 5 \times 10^{23} \text{ cm}^{-2}$. The reflected radiation arrives at the observer unabsorbed, or significantly less absorbed, than the intrinsic emission. The upper limit on the absorbing column density of the reflected component is

$N_{\text{H},z}^{\text{refl}} < 2.5 \times 10^{22} \text{ cm}^{-2}$ based on the Model 4 test. The reflecting material is neutral and located far from the black hole, as suggested by the width and energy of the fluorescent iron $K\alpha$ line, and the ionization parameter of the reflected component. When this best-fit model is applied to the *Swift/BAT* data, we find a normalization constant between the two data sets, $C_{\text{BAT}} = 0.68 \pm 0.10$.

The right panels in Figure 3 show data-to-model ratios (Models 1–3) in the *Swift/BAT* energy range. The figures indicate that the Model 3 scenario is favored and we plot the model and its components in Figure 5(a).

3.2. *XMM-Newton* Data

In this section we apply the best-fitting *Chandra* model (Model 3) to the *XMM-Newton* data.

Figure 4(a) shows the ratio of the *XMM-Newton* data to Model 3 with parameters fixed at the values best fitting the *Chandra* data. A soft excess below 2 keV is clearly visible, and is due to the diffuse emission of gas surrounding the nucleus collected from a large extraction region required by the *XMM-Newton* point-spread function. To account for this difference we thawed the temperature and normalization of the thermal bremsstrahlung component in Model 3 (kT and N_{TB} , respectively). The fit in the soft band improved significantly, although certain residuals indicative of emission/absorption lines were still present. Since we are interested primarily in the continuum AGN emission, we do not improve further on the soft (<2 keV) residuals and focus on modeling the spectrum at energies >2 keV. The resulting data-to-model ratios are plotted in Figure 4(b). The temperature kT is lower than in the case of the *Chandra* spectrum (although consistent within the uncertainties) and close to the temperature of the thermal

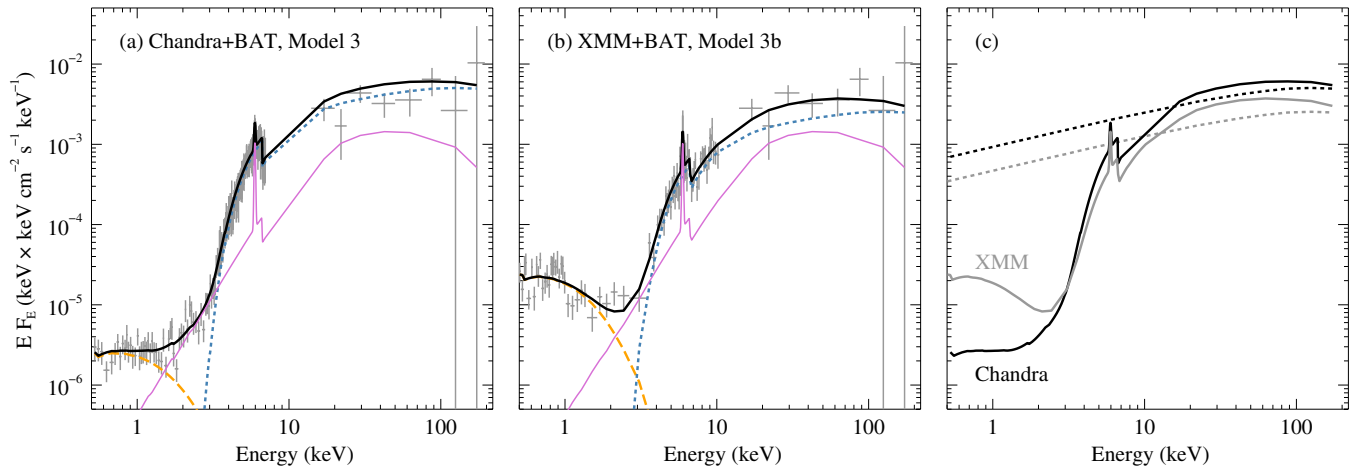


Figure 5. (a) Unfolded spectrum (*Chandra* and *Swift*/BAT, crosses) and best-fitting model (Model 3, thick solid/black). The model components are as follows: hard power-law emission (short-dash/blue) absorbed with an intrinsic column density $N_{H,z} \sim 5 \times 10^{23} \text{ cm}^{-2}$; reflected emission including the $\sim 6.4 \text{ keV}$ (rest-frame) iron $K\alpha$ line (thin solid/magenta); thermal diffuse emission (long-dash/orange); Galactic absorption. The *Chandra* data were grouped for clarity of the plot. (b) The same as (a) for *XMM-Newton* and *Swift*/BAT data (Model 3b). (c) Solid: best-fitting *Chandra* (black) and *XMM-Newton* (gray) total models. The enhanced soft diffuse emission in the *XMM-Newton* model is due to larger source extraction region than in the case of *Chandra*. Short-dash: unabsorbed power-law components with variable normalization responsible for the intrinsic X-ray variability of the source.

(A color version of this figure is available in the online journal.)

component in the *Chandra* background model. Residuals below and above $\sim 4 \text{ keV}$ are still apparent indicating that the intrinsic spectral properties of the nucleus might have changed between the *XMM-Newton* and *Chandra* observations. The shape of the residuals suggests that either the intrinsic absorption column varied (model excess below 4 keV) or the normalization of the power law varied (model deficit above 4 keV). We test both possibilities.

First we thaw the intrinsic absorption column (in addition to kT and N_{TB} ; Model 3a in Table 2) and repeat the fit. We obtain an increased intrinsic column density, $N_{H,z} \sim 8 \times 10^{23} \text{ cm}^{-2}$, with respect to that in the *Chandra* observation. The intrinsic EW is in agreement with that in *Chandra* Model 3, as expected, while the observed EW increases to $EW_o = 247 \pm 10 \text{ eV}$ (Table 2; Figure 4(c)). The fit resulted in $CSTAT = 228$ (191 degrees of freedom, dof).

Next, we test the hypothesis that the spectral variability is due to the variable normalization of the power law, N_{CPL} (Model 3b in Table 2; Figure 4(d)), while the intrinsic absorption and reflection parameters remain fixed at the values obtained from the analysis of the *Chandra* data. To correctly account for the constant absolute flux of the reflected component, we release the condition that the normalization of the reflected component is equal to the normalization of the power law. Instead, we fix the normalization of the reflected component at the value found in the *Chandra* data. We obtained $CSTAT = 209$ (191 dof). We find that N_{CPL} is lower by a factor ~ 2 in the *XMM-Newton* data than in the *Chandra* data. We note, however, that this parameter is subject to large errors in the *Chandra* data. This spectral variability scenario results in an increased EW of the iron line (observed $EW_o = 280 \pm 13 \text{ eV}$; intrinsic $EW_i = 122 \pm 6 \text{ eV}$) as compared with *Chandra* Model 3. A combined variability scenario (i.e., both $N_{H,z}$ and N_{CPL} allowed to vary; 190 dof) resulted in parameter values and $CSTAT$ consistent with those of Model 3b.

Finally, we checked the consistency between the *XMM-Newton* and *Swift*/BAT data. We found $C_{BAT} = 0.68 \pm 0.10$ and $C_{BAT} = 1.10 \pm 0.16$ in both cases, Models 3a and 3b, respectively. The data-to-model ratios in the *Swift*/BAT energy range are presented in Figures 4(c) and (d).

4. DISCUSSION

We studied the nuclear X-ray emission and X-ray spectral variability of a low-redshift radio galaxy, 4C+29.30, over a broad $0.5\text{--}200 \text{ keV}$ X-ray band using our deep $\sim 300 \text{ ks}$ *Chandra* observation, $\sim 17 \text{ ks}$ of cleaned *XMM-Newton* data, and archival 58 month catalog *Swift*/BAT data. We tested several spectral models, and concluded that Model 3 in Table 2 provides the best fit to our *Chandra* data supplemented by the *Swift*/BAT data. In this model the $2\text{--}200 \text{ keV}$ X-ray emission of the central AGN is decomposed into a strongly intrinsically obscured hard cutoff power-law continuum ($\Gamma \simeq 1.56$), and significantly less absorbed reprocessed emission including a neutral reflection hump and an accompanying neutral narrow iron $K\alpha$ line. The soft $0.5\text{--}2 \text{ keV}$ X-ray band is dominated by thermal diffuse emission, and may contain a marginal contribution of a scattered power-law component. The same model applied to the earlier *XMM-Newton* data led us to explore two X-ray variability scenarios. In the first one, the variability is apparent and caused by the variations of the intrinsic column density. In the other, the variability arises due to changes in the normalization of the power-law emission.

The hard X-ray spectrum, renewed nuclear radio activity (van Breugel et al. 1986; Jamrozy et al. 2007; Liuzzo et al. 2009), and weak optical continuum dominated by the host galaxy (van Breugel et al. 1986) suggest an analogy between the state of the nucleus in 4C+29.30 and a hard or hard-intermediate spectral state of Galactic black hole X-ray binaries (GBHs; see, e.g., Fender et al. 2004; Done et al. 2007). The spectral ages of large-scale radio structures in 4C+29.30 differ by $\sim 100 \text{ Myr}$. This timescale, when scaled down by the ratio between the black hole mass in 4C+29.30 ($\sim 10^8 M_\odot$, Section 4.4 of the present paper; Paper I) and that of a typical GBH ($\sim 10 M_\odot$), is comparable to the time between consecutive outbursts of GBHs ranging from years to decades (for examples of GBHs with at least two documented activity periods see, e.g., Table 1 in Remillard & McClintock 2006 and Figure 2 in Done et al. 2007). Thus, it is possible that we observed 4C+29.30 at an early stage of its renewed nuclear activity, which could have started as recently as several decades ago, judging by the spectral

age of the youngest nuclear radio structures. Interestingly, the age of the youngest radio structure, ~ 15 yr, found by Liuzzo et al. (2009) is in agreement with the suggestion of Jamroz et al. (2007) that a powerful outburst took place in 4C+29.30 in the period between 1990 and 2005. The X-ray loudness parameter (e.g., Zamorani et al. 1981; Avni & Tananbaum 1986), $\alpha_{\text{ox}} \simeq 0.3838(\log F_{\nu, \text{o}} - \log F_{\nu, \text{x}})$, where $F_{\nu, \text{o}}$ and $F_{\nu, \text{x}}$ are rest-frame flux densities at 2500 Å and 2 keV, respectively, can be calculated for 4C+29.30 assuming an AGN contribution to the optical band as in van Breugel et al. (1986), and 2 keV flux corrected for absorption (Model 3). We find a low value, $\alpha_{\text{ox}} \simeq 1$, further supporting the idea of a hard or hard-intermediate spectral state of the source (e.g., Sobolewska et al. 2009, 2011).

Below we discuss in detail the implications of our modeling on the nature of the studied AGN and its surroundings.

4.1. Origin of the X-Ray Spectral Variability

The three X-ray observations of 4C+29.30 available to date, spread over a period of several years, allow us to address the question of the X-ray variability of the source. The early *Chandra* data (2001 April; Gambill et al. 2003) were described with a simple power-law model (Γ fixed at 1.69) modified by Galactic absorption ($N_{\text{H}} = 4.06 \times 10^{20} \text{ cm}^{-2}$, slightly different than the value adopted in the present paper), and an intrinsic absorption $N_{\text{H},z} = 4.8^{+1.9}_{-1.4} \times 10^{23} \text{ cm}^{-2}$ in excellent agreement with that found in our new *Chandra* data, $N_{\text{H},z} = (4.96 \pm 0.15) \times 10^{23} \text{ cm}^{-2}$. The reported 2–10 keV absorbed flux was $1.1 \times 10^{-12} \text{ erg s}^{-1} \text{ cm}^{-2}$. Based on the Gambill et al. model parameters, we determined that the unabsorbed 2–10 keV flux of the source in 2001 April was $F_{\text{C},1} \simeq 4.8 \times 10^{-12} \text{ erg s}^{-1} \text{ cm}^{-2}$, comparable to that at the time of our *Chandra* observation, $F_{\text{C},2} = 4.7^{+0.3}_{-1.2} \times 10^{-12} \text{ erg s}^{-1} \text{ cm}^{-2}$ (2010 February). However, our deep observation revealed that the spectrum of the 4C+29.30 core is more complex due to the soft component and reflection features. The model of Gambill et al. (2003), when applied to our *Chandra* data, results in a reduction of the 2–10 keV flux, $F_{\text{C},2}$, by $\sim 6\%$. It is thus possible that $F_{\text{C},1}$ in Gambill et al. (2003) was underestimated by a few percent. Nevertheless, we conclude that the 2–10 keV flux and the properties of the intrinsic absorber were approximately unchanged between the two *Chandra* observations.

However, a discrepancy between our *Chandra* and *XMM-Newton* data (2008 April) is apparent, as demonstrated in Figure 4. We proposed two scenarios for the X-ray spectral variability of 4C+29.30. We started with the good quality deep *Chandra* observation to establish a baseline spectral model, and we found that the *XMM-Newton* data above 2 keV can be explained by varying only one spectral parameter: the intrinsic absorbing column density, $N_{\text{H},z}$, or the normalization of the power-law component, N_{CPL} . In the former case (variable $N_{\text{H},z}$), the *XMM-Newton* flux is in agreement with both *Chandra* measurements, $F_{\text{N},a} = F_{\text{C},2} \simeq F_{\text{C},1}$, while the intrinsic column density exceeds that measured with *Chandra* by $\sim 60\%$. In the latter case (variable N_{CPL}) we obtain $F_{\text{N},b} = (2.5 \pm 0.1) \times 10^{-12} \text{ erg s}^{-1} \text{ cm}^{-2} \simeq 0.53 F_{\text{C},2}$. Cross-calibration studies⁸ show that in general the spectra measured by *XMM-Newton* (EPIC/PN) and *Chandra* (ACIS-S) agree within 10% in the 0.5–2 keV band, and within 20% above 2 keV. Thus, the detected *Chandra* and *XMM-Newton* intrinsic flux difference is too high to be fully attributed to cross-calibration issues,

implying that in this scenario the source may be variable on timescales of several years in the 2–10 keV band.

Variations of the intrinsic column density seem to be a common phenomenon in AGNs on timescales as short as weeks (e.g., Risaliti et al. 2005, 2007, 2009, 2010). On the other hand, a non-variable narrow 6.4 keV iron line and associated constant neutral reflection not responding to the variations of the power-law component, interpreted as the reprocessing of the hard X-rays by a remote molecular torus, also seem to be common spectral features in both Type 1 AGNs (e.g., MCG-6-30-15, Vaughan & Fabian 2004; NGC 4051, Miller et al. 2010; Ponti et al. 2006; Mrk 841, Petrucci et al. 2007; Ark 120, Nardini et al. 2011; a sample of 14 Seyfert 1 galaxies, Bhayani & Nandra 2010) and Type 2 AGNs (e.g., a sample of 20 Seyfert 2 galaxies, Risaliti 2002; MCG-5-23-16, Reeves et al. 2006; NGC 2992, Yaqoob et al. 2007 and references therein; NGC 4945, Itoh et al. 2008; Marinucci et al. 2012).

In our modeling, both variability scenarios resulted in satisfactory fits (Table 2). However, a visual inspection of the fit residuals in the *XMM-Newton* and *Swift*/BAT energy ranges (Figure 4) seems to favor the scenario with variable power-law normalization, N_{CPL} (Model 3b), over the scenario with variable intrinsic column density, $N_{\text{H},z}$ (Model 3a). We confirmed that the model with variable N_{CPL} is more likely to be correct than the model with variable $N_{\text{H},z}$ by calculating the respective p -values (Protassov et al. 2002) based on a series of 1000 simulated data sets (using Sherpa’s `fake_pha` function) for two test cases: (1) variable $N_{\text{H},z}$ (null model) versus combined variability scenario (both $N_{\text{H},z}$ and N_{CPL} allowed to vary (alternative model) and (2) variable $N_{\text{H},z}$ (null model) versus combined variability scenario (alternative model). In case (1) we found a p -value $\ll 1 \times 10^{-3}$, which implied that the model with variable $N_{\text{H},z}$ is unlikely to be true. Conversely, in case (2) the high p -value = 0.32 suggests that the model with variable N_{CPL} is likely to be true.

In Figure 5(c) we show a comparison between the best-fitting *Chandra* and *XMM-Newton* total models, and the unabsorbed power-law model components in the case of the favored scenario with variable N_{CPL} .

4.2. Iron Line and Reflection Hump

The first short *Chandra* observation of 4C+29.30 contained too few counts to detect the iron $K\alpha$ line or put a limit on its EW (Gambill et al. 2003). Our *XMM-Newton* and *Chandra* observations are thus the first detections of the $K\alpha$ iron line in this object. The line was narrow ($\Delta E \sim 0.06$ keV) and centered at the rest-frame energy close to 6.4 keV. These line properties indicate that it originated in a neutral matter far away from the black hole, i.e., outer parts of an accretion disk or a dusty torus.

The *intrinsic* EW of the iron line, EW_i , measured in our *XMM-Newton* and *Chandra* data is in the ~ 70 –120 eV range, depending on the adopted variability scenario (Table 2). An iron line originating in a lamp-post model due to reprocessing of hard power-law X-rays with $\Gamma = 1.9$ by an accretion disk observed face-on has an expected EW of ~ 140 eV (e.g., George & Fabian 1991). However, this EW is sensitive to a number of parameters such as the photon index, viewing angle, iron abundance, and optical depth for electron scattering. Nandra et al. (2007) give the photon index and inclination-dependent formulae for the EW based on the fits to the Monte Carlo simulations of George & Fabian (1991). For $\Gamma \sim 1.56$ resulting from our fits and an assumed inclination of 45° , we obtain the predicted EW of ~ 170 eV. This value should be considered as an upper limit

⁸ <http://xmm2.esac.esa.int/docs/documents/CAL-TN-0052.ps.gz>

due to the unknown disk/X-ray source geometry (the reflection amplitude in our data is $|\Omega/2\pi| \sim 0.3$ which may suggest, e.g., a truncated disk geometry or a patchy corona, as opposed to $\Omega/2\pi = 1$ in the lamp-post model). It is thus possible that at least some of the photons forming an iron line with an (intrinsic) EW of 70–120 eV, as measured in this paper, originated in an accretion disk. This would require that the intrinsic absorber and the reflector were two separate media.

Ghisellini et al. (1994) presented a scenario in which the iron line is formed as a result of the reprocessing of a power-law continuum by a molecular torus (see also Krolik et al. 1994; Levenson et al. 2002). The torus scenario for the origin of the iron line provides a compelling possibility of associating the intrinsic absorber with the reflector. The EW of the iron line for tori with $N_{\text{H}} \sim (5-8) \times 10^{23} \text{ cm}^{-2}$ and a half-opening angle of $30^\circ-45^\circ$ is predicted in the $\sim 80-300$ eV range, with the lower (higher) values corresponding to the face-on (edge-on) view. Ghisellini et al. (1994) assumed an illuminating power law with $\Gamma = 1.9$. Levenson et al. (2002) estimated that the allowed range of EWs increases by up to 5% if the spectrum hardens with $\Gamma = 1.9$ changing to $\Gamma = 1.7$ (for intermediate viewing angles $i < 65^\circ$). The spectrum measured in our data is even harder, characterized with $\Gamma \sim 1.56$, which implies even larger allowed EWs. Comparing these predictions with the *observed* iron line EWs in 4C+29.30, we find that both *Chandra* and *XMM-Newton* measurements, $\text{EW}_o \sim 170-280$ eV, lie within the range predicted by the torus origin of the iron line.

In Model 3, we used the `pexriv+zgauss` model of X-ray reprocessing. We are aware of certain issues associated with this approach, which include the iron line added to a continuum in an arbitrary way, and the assumption that the hard X-rays are reflected by an accretion disk. We argue instead that the reflector could be associated with a molecular torus. Models of hard X-ray reprocessing by a toroidal reflector are available (Ghisellini et al. 1994; Krolik et al. 1994; Levenson et al. 2002; Murphy & Yaqoob 2009). Of these, the tabulated model `mytorus` of Murphy & Yaqoob (2009) accounts self-consistently for all components reprocessed by an optically thick torus—the zero-order absorbed component, the scattered component, and associated fluorescent Fe $K\alpha$, Fe $K\beta$, and Ni $K\alpha$ emission lines. However, the model in its present version considers a torus with a fixed half-opening angle of $\theta_{\text{MYT}} = 60^\circ$. This model tested on our *Chandra* data requires almost an edge-on view, $i = 85^\circ$, in contradiction with the viewing angle constraints based on the jet-to-counterjet flux ratio. The data of 4C+29.30 require that the zero-order component is strongly absorbed, indicating that the torus half-opening angle $\theta < i < 60^\circ$. With the viewing angle fixed at $i = 45^\circ$, an additional intrinsic absorber affecting only the zero-order component of the `mytorus` model is needed in order to obtain a good fit, which breaks the consistency of the model. We conclude that the available `mytorus` model does not provide enough flexibility at this time to account for the case appropriate for our source, in which $\theta < i < \theta_{\text{MYT}} = 60^\circ$.

4.3. 4C+29.30: A “Hidden” AGN

Recently, a new class of AGNs has been identified in the *Suzaku* and *XMM-Newton* follow-ups of the *Swift*/BAT AGNs with $N_{\text{H}} > 10^{23.5} \text{ cm}^{-2}$ (e.g., Ueda et al. 2007; Winter et al. 2008, 2009a, 2009b; Eguchi et al. 2009, 2011; Noguchi et al. 2009, 2010). The characteristic feature of these AGNs is a lower contribution of the scattered power-law emission to the soft X-ray band, $f_{\text{sc}} < 3\%$, as compared to that of typical Seyfert 2 galaxies, $f_{\text{sc}} = 3\%-10\%$ (e.g., Turner et al. 1997; Guainazzi

et al. 2005; Winter et al. 2009a; Noguchi et al. 2009, 2010). Winter et al. (2009a) found that 24% of their entire *Swift*/BAT-selected sample (153 sources) belong to this new class of AGNs based on the $f_{\text{sc}} < 3\%$ and low soft-to-hard X-ray observed flux ratio, $F_{0.5-2 \text{ keV}}/F_{2-10 \text{ keV}} < 0.04$. Ueda et al. (2007) proposed that the reduced f_{sc} is due to a geometrically thick torus covering a significant fraction of the solid angle. They predicted that in this new class of AGNs, the [O III] lines relative to hard X-ray luminosity would be weaker than in the typical Seyfert 2 galaxies because of lower flux arriving at the NLR in the presence of a geometrically thick torus. A term “hidden” or “buried” AGN was proposed for this new class, which was missed in previous optically and soft X-ray-selected samples.

Noguchi et al. (2009, 2010) identified hidden AGN candidates in the 2XMM Catalogue using X-ray hardness ratios, HR3 and HR4 (for definitions, see the 2XMM User Guide to the Catalogue). These two hardness ratios, calculated for the *XMM-Newton* data of 4C+29.30, HR3=0.09 and HR4=0.83, comply with the Noguchi et al. selection criteria. In our analysis, we found that the scattered component was not formally required to model the data and that the scattering fraction was consistent with zero (Model 6), $f_{\text{sc}} < 0.25 \times 10^{-2}$. This value is quite low but in agreement with f_{sc} found previously in several other Seyfert 2s (Ueda et al. 2007; Eguchi et al. 2009; Noguchi et al. 2009; Winter et al. 2009a, 2009b), and implies a torus with a half-opening angle $\theta \lesssim 20^\circ$ (Eguchi et al. 2009 for $f_{\text{sc}} < 0.5\%$). The observed soft-to-hard flux ratio in 4C+29.30 is $F_{0.5-2 \text{ keV}}/F_{2-10 \text{ keV}} \sim 0.005$. Thus, the *XMM-Newton* colors, f_{sc} , and soft-to-hard flux ratio indicate that 4C+29.30 is a hidden AGN candidate.

Noguchi et al. (2010) showed that the scattering fraction f_{sc} correlates with the ratio of the reddening corrected [O III] $\lambda 5007 \text{ \AA}$ line luminosity to the 2–10 keV intrinsic luminosity $\ell = L_{[\text{O III}] \lambda 5007} / L_{2-10 \text{ keV}}$. Thus, to further exploit the intriguing hidden AGN scenario in 4C+29.30, we investigated the properties of its [O III] emission line. We used the observed [O III] flux reported by van Breugel et al. (1986). We corrected it for the extinction using their observed H_α/H_β luminosity ratio of 5.1 and the relation of Bassani et al. (1999) with the assumed Galactic gas to dust ratio, i.e., $(H_\alpha/H_\beta)_0 = 3.1$. We obtained $\ell \sim 0.1$ in 4C+29.30, which means that our source can be placed somewhat above the Noguchi et al. correlation, however, within the scatter produced by the sources used to derive the correlation.

Based on a sample of six AGNs, Eguchi et al. (2009) speculated that hidden AGNs with $f_{\text{sc}} < 0.5\%$ have high reflection amplitudes $\Omega/2\pi \gtrsim 0.8$, while those with $0.5\% < f_{\text{sc}} < 3\%$ have $\Omega/2\pi \lesssim 0.8$. 4C+29.30 with $|\Omega/2\pi| = 0.32_{-0.05}^{+0.09}$ and $f_{\text{sc}} < 0.25\%$ fits in the gap between the two groups in the $\Omega/2\pi$ versus f_{sc} diagram (similar to two other sources in Eguchi et al. 2011), indicating that the distribution of f_{sc} and $\Omega/2\pi$ may be continuous rather than split into two distinct groups.

The soft thermal emission identified in our *Chandra* image contributes the majority of the 0.5–2 keV flux. However, this component may be easily overlooked in the data with lower exposure or spatial resolution. We investigated a possible effect of neglecting this component in the total model (Model 7 in Table 1). We found that the most striking difference between Model 3 and Model 7 is the softening of the photon index in the case without the thermal component, $\Gamma_{\text{M7}} = 2.03 \pm 0.16$. This follows from the adjustment of the slope of the scattered unabsorbed component (linked in the model to that of the CPL) in order to account for the soft X-ray emission but not to overestimate the hard X-rays at the same time.

We conclude that more detailed studies of the soft emission in the hidden AGN complemented by better quality hard X-ray data (e.g., NuSTAR) are of particular importance to recognizing their X-ray properties and geometry of the obscuring torus.

4.4. Black Hole Mass

Noguchi et al. (2010) showed that the scattering fraction, f_{sc} , anti-correlates with the Eddington luminosity ratio, L_{bol}/L_E , where $L_{bol} \simeq 30 \times L_{2-10\text{keV}}^{CPL}$ (applying a bolometric correction factor of 30 typical for luminous AGNs; e.g., Vasudevan & Fabian 2007). For 4C+29.30 the limit we found on the scattering fraction translates into $L_{bol}/L_E \gtrsim 0.1$, which gives $M_{BH} \lesssim 1.2 \times 10^8 M_\odot$.

Another black hole mass estimate can be done using the empirical relation between M_{BH} and stellar velocity dispersion, σ_* (Tremaine et al. 2002). Based on the optical spectrum taken from the Sloan Digital Sky Survey (SDSS) Data Release 7 (Abazajian et al. 2009) the stellar velocity dispersion of 4C+29.30 is $\sigma_* = 207.6 \text{ km s}^{-1}$ (using the STARLIGHT synthesis code of Cid Fernandes et al. 2005), resulting in a black hole mass $M_{BH} = 1.6 \times 10^8 M_\odot$.

These two new black hole mass estimates are compatible with the discussion presented in Paper I where $M_{BH} \gtrsim 10^8 M_\odot$ was found based on an argument involving energetics of the system. Thus, it is possible that the mass of the black hole in 4C+29.30 is close to $10^8 M_\odot$.

4.5. Multiwavelength Perspective of 4C+29.30

4.5.1. Infrared

X-ray radiation absorbed and reprocessed by an obscuring torus would eventually emerge in the infrared band. Models of the infrared AGN spectral energy distributions under the assumption of a clumpy structure of a molecular torus (Nenkova et al. 2002, 2008a, 2008b; Hönig et al. 2006) are potentially able to constrain the torus geometry in sources observed in IR with a high spatial resolution (e.g., Gandhi et al. 2009; Alonso-Herrero et al. 2012), with the near-IR 1–5 μm fluxes being most sensitive to the inclination effects (Nenkova et al. 2008b). 4C+29.30 was observed in infrared by IRAS, 2MASS, and WISE, of which the two latter surveys sampled the desired near-IR band. However, in 4C+29.30 the 2MASS measurements are dominated by the host galaxy,⁹ while the WISE observations with a spatial resolution of 6''–12'' correspond to our 10'' *Chandra* background region rather than the core region. Nevertheless, we use the W2 and W3 filters at rest-frame wavelengths $\lambda_{W2} \sim 4.2 \mu\text{m}$ and $\lambda_{W3} \sim 11.3 \mu\text{m}$, to constrain the viewing angle of our source. We calculated respective $f = \nu F_\nu / F_{bol}$ ratios (where F_{bol} corresponds to $L_{bol} \sim 10^{45} \text{ erg s}^{-1}$) and compared them with the 4.5 μm and 12 μm models of Nenkova et al. (2008b, Figure 10; see also Erratum in Nenkova et al. 2010). We obtained $f_{4.3\mu\text{m}} \simeq 0.06$ and $f_{11.3\mu\text{m}} \simeq 0.08$, which gave $i \simeq 70^\circ$ and no constraint (our $f_{11.3\mu\text{m}}$ was too low to intercept the 12 μm model of Nenkova et al. 2008b), in contradiction with the $i < 60^\circ$ condition followed from the jet-to-counterjet flux ratio. The $f_{4.3\mu\text{m}}$ and $f_{11.3\mu\text{m}}$ ratios are a factor of 2–6 too low to comply with the $i < 60^\circ$ constraint. There are several reasons for this discrepancy to consider. (1) The bolometric luminosity of 4C+29.30 might have

been underestimated by a factor of a few due to the uncertainty of the applied bolometric correction. (2) The geometry of the obscuring torus may differ from that considered in Nenkova et al. (2008b), e.g., the case of a geometrically thick torus with half-opening angle $\lesssim 20^\circ$ evoked for hidden AGNs by Eguchi et al. (2009) would imply a torus width parameter $\sigma \gtrsim 70^\circ$ (see Figure 1 in Nenkova et al. 2008b for the illustration of σ) as opposed to $\sigma = 45^\circ$ assumed to compute the models. (3) Finally, the $\sim 12 \mu\text{m}$ WISE flux might be partially affected by the 4C+29.30 ISM environment (see, e.g., Goulding et al. 2012 for arguments in favor of a host galaxy origin of the rest-frame 9.7 μm Si-absorption feature in Compton-thick Seyfert 2 galaxies), e.g., a dust lane covering the central part of the nucleus, clearly visible in the archival *HST* image in Figure 2.

We verified the third scenario using the correlation reported in Gandhi et al. (2009) for a number of Seyfert 2 galaxies between their 2–10 keV luminosities and 12 μm luminosities. The IR luminosities in Gandhi et al. (2009) follow from subarcsecond resolution observations, and thus they are most likely representative of the true IR nuclear emission. In 4C+29.30 the $\sim 12 \mu\text{m}$ luminosity is $L_{12\mu\text{m}} \sim 8.3 \times 10^{43} \text{ erg s}^{-1}$. This is in agreement with the expected $L_{12\mu\text{m}} \sim 8.8^{+2.2}_{-1.8} \times 10^{43} \text{ erg s}^{-1}$ (based on our unabsorbed 2–10 keV *Chandra* flux, Model 3), leaving scenarios (1) and/or (2) as plausible causes of the discrepancy between the Nenkova et al. (2008b) models and 4C+29.30 WISE flux measurements.

4.5.2. Radio

4C+29.30 is an intermittent radio galaxy with evidence for several jet ejection events with the spectral time ranging from $\gtrsim 200 \text{ Myr}$ (the relic structure), through $\lesssim 100 \text{ Myr}$ and $\lesssim 33 \text{ Myr}$, to $\sim 15 \text{ yr}$ and $\sim 70 \text{ yr}$ (Jamrozy et al. 2007; Liuzzo et al. 2009). However, the radio activity of 4C+29.30 seems rather mild in comparison with the powerful radio sources. The total jet power of 4C+29.30, $L_j \sim 10^{42} \text{ erg s}^{-1}$, constitutes only a small fraction of its Eddington luminosity, $L_j \sim 10^{-4} L_E$, while in the most powerful blazars L_j reaches $(0.1\text{--}1)L_E$ (e.g., Ghisellini et al. 2009). Low-power FR I radio galaxies are characterized by much lower values of L_j/L_E (e.g., $\sim 10^{-3}$ in the case of M87), but at the same time they accrete at low rates ($L_{bol}/L_E \ll 0.1$) probably in a radiatively inefficient mode. On the contrary, we estimated that the Eddington luminosity ratio of our low-power radio galaxy is quite substantial, $L_{bol} \gtrsim 0.1 L_E$.

The standard radio loudness parameter is typically defined as the ratio of 5 GHz radio to *B*-band (4400 Å) optical luminosity spectral densities, $R \equiv L_{\nu,R}/L_{\nu,B}$, with $R > 10$ characterizing radio-loud AGNs (as proposed for quasars by Kellermann et al. 1989). In the case of 4C+29.30, one can calculate $90 \lesssim R \lesssim 430$ based on the available archival data (5 GHz total flux given in Liuzzo et al. 2009 and 4400 Å flux extrapolated from the allowed range of the 5400 Å nuclear flux, assuming $\alpha_{opt} = 1.2$; see the discussion in van Breugel et al. 1986). However, this value should be taken with caution mainly because of uncertainties associated with the attenuation of the optical nuclear flux due to the obscured nature of the source, and host galaxy contribution known to be particularly relevant in the case of low-power Seyfert galaxies (Ho & Peng 2001; Sikora et al. 2007).

We compared the radio properties of 4C+29.30 with those of 52 hidden AGN candidates compiled from the literature based on Ueda et al. (2007), Eguchi et al. (2009, 2011), Noguchi et al. (2009, 2010), and Winter et al. (2009a, 2009b). In approximately one-third of them (17 of 52) the scattered

⁹ We estimated the host galaxy contribution to the *J*, *H*, and *K*, bands using the flux measurement at 5400 Å being a sum of $\lesssim 80\%$ and $\gtrsim 20\%$ galaxy and AGN emission, respectively (van Breugel et al. 1986), the $E(B - V) = 0.5$ mag reddening possibly due to a dust lane (van Breugel et al. 1986), and the 10 Gyr elliptical galaxy template of Buzzoni (2005).

fraction was reported to be $\lesssim 0.5\%$ in at least one publication, that is, at a level comparable with the upper limit estimated in 4C+29.30, implying a geometrically thick torus with an opening angle $\lesssim 20^\circ$ (Eguchi et al. 2009). Combination of the available archival NVSS (Condon et al. 1998) and NED data allowed us to calculate the standard radio loudness parameter in the case of 34 sources, including 14 of 17 sources with $f_{sc} < 0.5\%$. We found that approximately one-third of these sources (11 of 34) could be considered radio-loud according to the condition $R > 10$. Among them we distinguished five radio-intermediate sources with $R \sim 10\text{--}20$, and six sources with a substantially higher radio loudness, $R \sim (2\text{--}27) \times 10^3$. We caution, however, that similar to the case of 4C+29.30, the calculated values of the radio loudness are only approximate due to the obscured nature of the hidden AGN. Nonetheless, it seems that the hidden nuclei are associated predominantly with the radio-quiet AGN.

Finally, we stress that among the 34 sources with measured radio loudness, R , we found only three ($\sim 9\%$) with $f_{sc} < 0.5\%$ and $R > 10$ (Mrk 348, 3C 33, and NGC 612). Hence, 4C+29.30 appears quite unusual in that it shows properties characteristic to both radio-loud AGNs and hidden AGNs with extremely geometrically thick tori. Based on the present data it cannot be determined whether a small fraction of radio-loud AGNs among the hidden AGN population is due to physical constraints or an observational bias.

5. CONCLUSIONS

We confirmed that the X-ray emission of the AGN in 4C+29.30, a radio source hosted by an elliptical galaxy, resembles Seyfert 2 type activity. We estimated that the mass of the central black hole is of the order of $10^8 M_\odot$. We decomposed the broadband 0.5–200 keV X-ray continuum (*Chandra/XMM-Newton* supplemented by *Swift*/BAT observations) into (1) a hard ($\Gamma = 1.5\text{--}1.6$) cutoff power-law component attenuated due to a strong intrinsic X-ray absorption with column density $N_{\text{H}} \sim 5 \times 10^{23} \text{ cm}^{-2}$, (2) a reflection hump ($|\Omega/2\pi| \sim 0.3$) and narrow iron $K\alpha$ line detected for the first time in this source originating due to the reprocessing of the AGN power-law emission by a distant neutral matter, (3) soft thermal emission of a diffuse gas clearly detected in our *Chandra* image dominating the 0.5–2 keV band, and (4) a marginal contribution of a scattered power-law emission to the soft X-ray band, $f_{sc} < 0.25\%$. We hypothesized that both the distant reflector and the obscuring matter can be associated with a molecular torus. Based on f_{sc} , the ratio of the observed soft-to-hard X-ray fluxes, and the *XMM-Newton* colors, we proposed that 4C+29.30 belongs to the hidden/buried AGNs, a new class that is emerging among the *Swift*/BAT hard X-ray-selected AGNs. We demonstrated that 4C+29.30, a radio-loud source with an intermittent jet activity and f_{sc} below 0.5%, shows properties characteristic of only $\sim 9\%$ of the presently identified hidden/buried AGN candidates with estimated radio loudness parameters.

We thank the anonymous referee for careful reading of our manuscript and comments that led to its improvement. Ł.S. is grateful for the support from Polish MNiSW through the grant No. N203-380336. M.J. was supported by Polish MNiSW funds for scientific research in years 2009–2012 under the Contract No. 3812/B/H03/2009/36. Work at NRL (C.C.C.) is sponsored by NASA DPR S-15633-Y. This research has made use of data obtained with the *Chandra X-Ray Observatory* and *Chandra X-Ray Center* (CXC) in the application packages CIAO, ChIPS,

and Sherpa. This research is funded in part by NASA contract NAS8-39073. Partial support for this work was provided by the *Chandra* grants, GO0-11133X and GO1-12145X, and *XMM-Newton* grant NNX08AX35G.

REFERENCES

- Abazajian, K. N., Adelman-McCarthy, J. K., Agüeros, M. A., et al. 2009, *ApJS*, **182**, 543
- Alonso-Herrero, A., Pereira-Santaella, M., Rieke, G. H., & Rigopoulou, D. 2012, *ApJ*, **744**, 2
- Arnaud, K. A. 1996, in ASP Conf. Ser. 101, *Astronomical Data Analysis Software and Systems V*, ed. G. H. Jacoby & J. Barnes (San Francisco, CA: ASP), 17
- Avni, Y., & Tananbaum, H. 1986, *ApJ*, **305**, 83
- Bassani, L., Dadina, M., Maiolino, R., et al. 1999, *ApJS*, **121**, 473
- Baumgartner, W. H., et al. 2010, *ApJS*, submitted (<http://heasarc.nasa.gov/docs/swift/results/bs58mon/>)
- Bhayani, S., & Nandra, K. 2010, *MNRAS*, **408**, 1020
- Buzzoni, A. 2005, *MNRAS*, **361**, 725
- Cid Fernandes, R., Mateus, A., Sodré, L., Stasińska, G., & Gomes, J. M. 2005, *MNRAS*, **358**, 363
- Condon, J. J., Cotton, W. D., Greisen, E. W., et al. 1998, *AJ*, **115**, 1693
- Dickey, J. M., & Lockman, F. J. 1990, *ARA&A*, **28**, 215
- Done, C., Gierliński, M., & Kubota, A. 2007, *A&ARv*, **15**, 1
- Eguchi, S., Ueda, Y., Awaki, H., et al. 2011, *ApJ*, **729**, 31
- Eguchi, S., Ueda, Y., Terashima, Y., Mushotzky, R., & Tueller, J. 2009, *ApJ*, **696**, 1657
- Evans, D. A., Lee, J. C., Turner, T. J., Weaver, K. A., & Marshall, H. L. 2007, *ApJ*, **671**, 1345
- Evans, D. A., Reeves, J. N., Hardcastle, M. J., et al. 2010, *ApJ*, **710**, 859
- Fabian, A. C., Sanders, J. S., Williams, R. J. R., et al. 2011, *MNRAS*, **417**, 172
- Fender, R. P., Belloni, T. M., & Gallo, E. 2004, *MNRAS*, **355**, 1105
- Freeman, P., Doe, S., & Siemiginowska, A. 2001, *Proc. SPIE*, **4477**, 76
- Gambill, J. K., Sambruna, R. M., Chartas, G., et al. 2003, *A&A*, **401**, 505
- Gandhi, P., Horst, H., Smette, A., et al. 2009, *A&A*, **502**, 457
- George, I. M., & Fabian, A. C. 1991, *MNRAS*, **249**, 352
- Ghisellini, G., Haardt, F., & Matt, G. 1994, *MNRAS*, **267**, 743
- Ghisellini, G., Tavecchio, F., & Ghirlanda, G. 2009, *MNRAS*, **399**, 2041
- Goulding, A. D., Alexander, D. M., Bauer, F. E., et al. 2012, *ApJ*, **755**, 5
- Grandi, P., Guainazzi, M., Cappi, M., & Ponti, G. 2007, *MNRAS*, **381**, L21
- Guainazzi, M., Matt, G., & Perola, G. C. 2005, *A&A*, **444**, 119
- Ho, L. C., & Peng, C. Y. 2001, *ApJ*, **555**, 650
- Hönig, S. F., Beckert, T., Ohnaka, K., & Weigelt, G. 2006, *A&A*, **452**, 459
- Itoh, T., Done, C., Makishima, K., et al. 2008, *PASJ*, **60**, 251
- Jamrozny, M., Konar, C., Saikia, D. J., et al. 2007, *MNRAS*, **378**, 581
- Kellermann, K. I., Sramek, R., Schmidt, M., Shaffer, D. B., & Green, R. 1989, *AJ*, **98**, 1195
- Kim, D.-W. 2012, *Astrophys. Space Sci. Libr.*, **378**, 121
- Krolik, J. H., Madau, P., & Życki, P. T. 1994, *ApJ*, **420**, L57
- Levenson, N. A., Krolik, J. H., Życki, P. T., et al. 2002, *ApJ*, **573**, L81
- Liuzzo, E., Giovannini, G., Giroletti, M., & Taylor, G. B. 2009, *A&A*, **505**, 509
- Magdziarz, P., & Zdziarski, A. A. 1995, *MNRAS*, **273**, 837
- Marinucci, A., Risaliti, G., Wang, J., et al. 2012, *MNRAS*, **423**, L6
- Miller, L., Turner, T. J., Reeves, J. N., et al. 2010, *MNRAS*, **403**, 196
- Million, E. T., Werner, N., Simionescu, A., et al. 2010, *MNRAS*, **407**, 2046
- Morganti, R. 2010, *PASA*, **27**, 463
- Murphy, K. D., & Yaqoob, T. 2009, *MNRAS*, **397**, 1549
- Nandra, K., O’Neill, P. M., George, I. M., & Reeves, J. N. 2007, *MNRAS*, **382**, 194
- Nardini, E., Fabian, A. C., Reis, R. C., & Walton, D. J. 2011, *MNRAS*, **410**, 1251
- Lenkova, M., Ivezić, Ž., & Elitzur, M. 2002, *ApJ*, **570**, L9
- Lenkova, M., Sirocky, M. M., Ivezić, Ž., & Elitzur, M. 2008a, *ApJ*, **685**, 147
- Lenkova, M., Sirocky, M. M., Nikutta, R., Ivezić, Ž., & Elitzur, M. 2008b, *ApJ*, **685**, 160
- Lenkova, M., Sirocky, M. M., Nikutta, R., Ivezić, Ž., & Elitzur, M. 2010, *ApJ*, **723**, 1827
- Noguchi, K., Terashima, Y., & Awaki, H. 2009, *ApJ*, **705**, 454
- Noguchi, K., Terashima, Y., Ishino, Y., et al. 2010, *ApJ*, **711**, 144
- Petrucci, P. O., Ponti, G., Matt, G., et al. 2007, *A&A*, **470**, 889
- Ponti, G., Miniutti, G., Cappi, M., et al. 2006, *MNRAS*, **368**, 903
- Protassov, R., van Dyk, D. A., Connors, A., Kashyap, V. L., & Siemiginowska, A. 2002, *ApJ*, **571**, 545
- Reeves, J. N., Fabian, A. C., Kataoka, J., et al. 2006, *Astron. Nachr.*, **327**, 1079
- Remillard, R. A., & McClintock, J. E. 2006, *ARA&A*, **44**, 49

- Risaliti, G. 2002, *A&A*, **386**, 379
- Risaliti, G., Elvis, M., Bianchi, S., & Matt, G. 2010, *MNRAS*, **406**, L20
- Risaliti, G., Elvis, M., Fabbiano, G., Baldi, A., & Zezas, A. 2005, *ApJ*, **623**, L93
- Risaliti, G., Elvis, M., Fabbiano, G., et al. 2007, *ApJ*, **659**, L111
- Risaliti, G., Salvati, M., Elvis, M., et al. 2009, *MNRAS*, **393**, L1
- Sambruna, R. M., Gambill, J. K., Maraschi, L., et al. 2004, *ApJ*, **608**, 698
- Siemiginowska, A., Stawarz, Ł., Cheung, C. C., et al. 2012, *ApJ*, **750**, 124 (Paper I)
- Sikora, M., Stawarz, Ł., & Lasota, J.-P. 2007, *ApJ*, **658**, 815
- Sobolewska, M. A., Gierliński, M., & Siemiginowska, A. 2009, *MNRAS*, **394**, 1640
- Sobolewska, M. A., Siemiginowska, A., & Gierliński, M. 2011, *MNRAS*, **413**, 2259
- Tremaine, S., Gebhardt, K., Bender, R., et al. 2002, *ApJ*, **574**, 740
- Turner, T. J., George, I. M., Nandra, K., & Mushotzky, R. F. 1997, *ApJ*, **488**, 164
- Ueda, Y., Eguchi, S., Terashima, Y., et al. 2007, *ApJ*, **664**, L79
- Urry, C. M., & Padovani, P. 1995, *PASP*, **107**, 803
- van Breugel, W. J. M., Heckman, T. M., Miley, G. K., & Filippenko, A. V. 1986, *ApJ*, **311**, 58
- Vasudevan, R. V., & Fabian, A. C. 2007, *MNRAS*, **381**, 1235
- Vaughan, S., Edelson, R., Warwick, R. S., & Uttley, P. 2003, *MNRAS*, **345**, 1271
- Vaughan, S., & Fabian, A. C. 2004, *MNRAS*, **348**, 1415
- Winter, L. M., Mushotzky, R. F., Reynolds, C. S., & Tueller, J. 2009a, *ApJ*, **690**, 1322
- Winter, L. M., Mushotzky, R. F., Terashima, Y., & Ueda, Y. 2009b, *ApJ*, **701**, 1644
- Winter, L. M., Mushotzky, R. F., Tueller, J., & Markwardt, C. 2008, *ApJ*, **674**, 686
- Yaqoob, T., Murphy, K. D., Griffiths, R. E., et al. 2007, *PASJ*, **59**, 283
- Zamorani, G., Henry, J. P., Maccacaro, T., et al. 1981, *ApJ*, **245**, 357